High Frequency Characterization of Losses in Fully Assembled Stators of Slotless PM Motors

Jonas Millinger, *Student Member*, *IEEE*, Oskar Wallmark, *Member*, *IEEE*,
and Juliette Soulard, *Member*, *IEEE*

***Abstract*—The recent emerge of wide band-gap (WBG) power transistors enables higher switching frequencies in electrical motor drives. Their full utilization from a system point of view requires quantification of the corresponding time-harmonic motor losses. As an initial step, this paper presents a unique study of stator losses for three different commercially available non-oriented silicon-iron (SiFe) steel grades (with lamination thicknesses 0.1, 0.2 and 0.3 mm). The investigations cover a wide frequency range (10-100 kHz) at different levels of DC-bias (up to 1.6 T). Iron losses are identified from measurements on fully assembled stators, deploying a novel technique. By utilizing fully assembled stators, no additional samples are required. Manufacturing influence is inherently incorporated. Results show that measured iron losses are twice as high at 10 kHz compared to Epstein test results, which emphasizes the need to incorporate manufacturing influence on iron losses at high frequencies. The level of DC-bias is also observed to have a significant impact on iron losses (up to 30 %). Even though thinner laminations are known for reducing iron losses, the reduction is much lower than anticipated in the studied frequency range due to skin effect. Using 0.1 mm lamination gauge instead of 0.3 mm reduces losses by 50 % at 10 kHz, while the same substitution at 100 kHz only reduces losses by 30 %. Future work includes loss separation in complete converter-fed machines.**

***Index Terms*—Permanent magnet machines, magnetic losses, harmonic analysis, wide band gap semiconductors.**

I. Introduction

SLOTLESS electrical motors are preferred in applications with elevated demands on high efficiency and low weight, such as compressors, turbines, medical equipment and industrial hand tools [1]–[6]. Such applications often require advanced motor control, which is achieved by connection to a pulse-width modulated (PWM) power-electronic converter. The converter PWM output voltage not only contains the desired fundamental component, but also a set of undesired high-frequency harmonics, located around multiples of the switching frequency [7]. These harmonic voltage components contribute to undesired motor heating with reduced performance as consequence. Even though the issue of harmonic losses is not limited to only high speed machines, they suffer from a higher proportion of these losses due to their lower inductance [8]. A conventional solution is to add a large and costly inductive filter in order to suppress the harmonic currents fed to the motor, increasing system complexity and size.

Manuscript received September 26, 2017; revised December 22, 2017; accepted January 25, 2018. Corresponding author: J. Millinger (email: jonasmil@kth.se)

However, the recent emerge of wide band-gap (SiC and GaN) transistors have enabled significantly higher switching frequencies than their silicon-based counterparts [9]. This leads to reduced harmonic motor losses (see Table II in Section II and [10]–[12]). As discussed in Section II, this may enable a reduction (or complete elimination) of the required filter, resulting in smaller and less complex systems.

In order to optimize motor systems deploying wide band-gap power semiconductors, accurate models for harmonic losses in the motor are required at the design stage. In [13], the authors of the present paper developed an innovative experimental procedure with locked rotor and pulsating current. The method assumes harmonic superposition of each frequency component. Segregation of rotor losses in measurements on complete motors require accurate stator loss models.

Stator losses include winding and core (iron) losses. The latter may represent a significant share at higher frequencies. Even though the issue of iron loss prediction has been an active research topic for more than a century, no universal iron loss model is currently available [14]. Manufacturers often provide Epstein frame loss data up to 10 kHz on request, but little is known about iron losses in SiFe steel at higher frequencies. The few available studies [15]–[17] conclude that classical analytical iron loss approaches become increasingly inaccurate with frequency due to skin effect. No useful study regarding the impact of lamination thickness on iron losses in SiFe steel beyond 10 kHz could be found in the literature today.

Yet, full utilization of wide band-gap transistors in electric motor drives requires iron loss characterization up to hundreds of kHz. Conventional iron loss measurement techniques such as the Epstein-frame and the ring-core methods, require complex hardware and waveform control beyond a few kHz [17], [18]. Further, their neglect of complex field patterns and material deterioration due to manufacturing influences such as cutting, stacking and welding [19]–[22] limits the usefulness of such results. Another important aspect that requires attention is the influence of DC-bias magnetic field. The results in [23] and [24] report a significant impact of DC-bias on iron losses in SiFe steel below 1 kHz. Therefore, a similar study is required for the frequency range considered in this paper.

This paper presents a unique study of losses arising in fully assembled stator steel grades [25] of different gauges (0.1–0.3 mm) in a slotless 2-pole permanent-magnet motor. Losses are identified under sinusoidal, pulsating magnetic field in the high frequency range (10-100 kHz) at different levels of DC magnetization (up to $\approx$ 1.6 T). In order to predict the cross-sectional flux-density distribution necessary for loss

separation, the stator steel B-H curves are experimentally characterized. The winding losses are successfully identified using an innovative method. The harmonic magnetic flux density distribution is determined by small signal modeling of the core. Static 2D FEA can be used, thus yielding minimal computational effort. The DC-bias is created using an external excitation coil. By utilizing fully assembled stators, no additional core samples are needed. Manufacturing influences are inherently incorporated. As discussed in Section V, the large air gap reluctance eliminate the need for active current control. The method is of direct importance for the harmonic loss characterization of slotless motors. It also complements the studies studies considering manufacturing influence on iron losses.

An early version of this work [7] was presented at the International Electrical Machines and Drives Conference (IEMDC) 2017. This paper extends [7] with the following contributions: **a)** An application description including experimental motor loss data for switching frequencies in the range 8–40 kHz using a SiC-based inverter (see Section II); **b)** An extensive literature review (see sections III–IV); **c)** Experimental minor loop B-H characterization at different levels of DC-bias (see Section VII); **d)** A comprehensive study on the impact of DC bias on iron losses (see Section IX). **e)** A model sensitivity analysis (see Section X).

The paper is organized as follows. The motor under study is presented in Section II. The analytical winding loss model required for loss separation is introduced in Section III while the iron loss modelling is treated in Section IV. The method and measurement setup are described in Sections V and VI, respectively. The minor loop B-H curves of the investigated stator steels at different level of DC-bias are characterized in Section VII. The proposed winding loss models are validated in Section VIII. Iron loss results are presented in Section IX. The implications of the results as well as the model validity is discussed in Section X. Finally, conclusions are drawn in Section XI.

II. Investigated Motor

The motor under study is used in commercially available, handheld industrial nutrunners. In contrast to their domestic counterparts, industrial nutrunners have exceptional demands on reliability as well as ergonomics due to their high degree of utilization. Cooling fans are considered a life-time limiter in dirty industrial environments, and therefore not to prefer. Instead, reliable high performance industrial nutrunners require high efficiency. One successful method is to deploy a slotless motor design [5], enabling high rotational speeds and thereby high power density. Cogging torque is minimized by using a 2-pole ring-magnet rotor, with improved position control capability as consequence.

The radial cross-section of the investigated motor is presented in Fig. 1. The solid shaft is represented by the innermost layer. The shaft carries a layer of axially segmented ring magnets with parallel magnetization. The rotor is surrounded by an airgap followed by the copper windings. The copper windings are fixed by varnish inside the cylindrical, axially

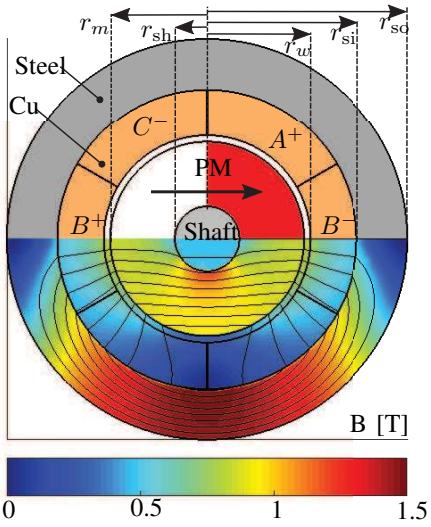

Fig. 1. Geometry and static magnetic field lines of the motor under study at no-load.

TABLE I
Key Motor Parameters.

Quantity	Symbol	Value
Peak torque	T_{max}	1.15 Nm
Max speed	n_{max}	30 krpm
DC bus voltage	U_{DC}	325 V
Number of phase turns	N	65
Motor active length	L_a	64.5 mm
Stator outer radius	r_{so}	15.5 mm
Stator yoke inner radius	r_{si}	11.6 mm
Winding inner radius	r_w	8 mm
Magnet radius	r_m	7.5 mm
Shaft radius	r_{sh}	2.5 mm
Nominal lamination thickness	h_{lam}	0.2 mm

laminated stator yoke. The laminations are supported by 8 straight, equally distributed axiperipheral welding seams, each ranging the whole active length. The nominal composition of the steel material under study in this paper is 3 % silicon and 0.4 % aluminum per weight unit. Further material data can be found in [25]. The relevant motor data is summarized in Table I. The stator is finally glued inside a motor house.

Fig. 2 shows the typical nutrunner load profile. It can be divided into: a) *the rundown*; followed by b) *the tightening*. Rundown is characterized by high speed and low torque, whereas tightening is distinguished by low speed and high torque. At tightening, copper losses are dominant, while magnetic losses dominate at rundown [26]. Traditionally, tightening losses have been dominant. Nevertheless, improved motor control techniques enable higher tightening speeds with reduced tightening losses as consequence. Instead, rundown losses are becoming the dominant loss source in many applications, and their reduction is gaining emphasis for improved nutrunner performance.

Even though the mechanical work conducted during rundown is negligible, the related power losses are often significant due to the poor efficiency at this operating point. The power losses at rundown can be represented by the no-load losses. They can further be divided into fundamental (P_0) and

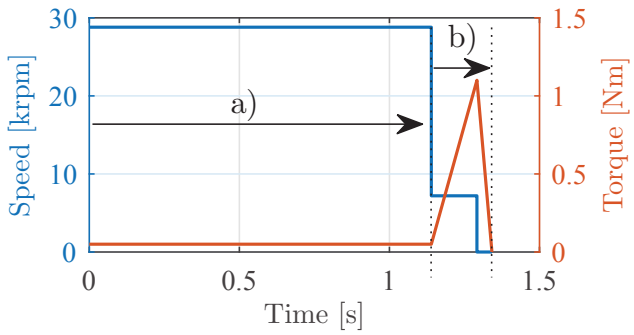

Fig. 2. Typical load profile of an electric motor for handheld nutrunners: a) rundown ($T_{\text{rundown}} \approx 1.15s$); b) tightening ($T_{\text{tightening}} \approx 0.2s$).

TABLE II
MEASURED MOTOR NO-LOAD LOSSES AT 30 KRPM [12].

P \ f_{sw}	8 kHz	20 kHz	40 kHz
P_0	16 W	16 W	16 W
P_h	31.1 W	19.7 W	13.8 W

harmonic (P_h) losses according to: $P_{\text{no-load}} = P_0 + P_h$. Fundamental losses P_0 are independent of the supply waveform, whereas the harmonic ones P_h depend on the inverter supply waveform. Due to the absence of stator slots, and negligible amount of winding space harmonics in the motor under study [27], the harmonic losses are essentially caused by the time harmonics of the input voltage PWM.

In its industrial application, the motor is fed by a three-phase power electronic inverter with a 325 V DC-bus via an inductive filter. The weight of the inductive filter equals the combined weight of the motor and power-electronic module [12]. Therefore, its elimination is highly desired. Typical rundown motor losses (at 30 krpm no-load, using 8 kHz switching frequency) are around 23.5 W, of which 7.5 W are harmonic losses [12]. The Fourier separation of power losses into fundamental and harmonic ones is thoroughly described in [12], using voltage and current harmonic spectra.

By using wide band-gap transistors, switching frequencies of up to 50 kHz are considered possible [9]. Table II shows the measured *fundamental* and *harmonic* motor losses at 30 krpm no-load operation *without* using the filter at three different switching frequencies (f_{sw}). As can be seen, fundamental losses are independent of the switching frequency while harmonic losses can be more than halved by using 40 kHz instead of 8 kHz switching frequency. However, full utilization of wide band-gap transistors in electrical motor drives require accurate models for harmonic motor losses. The time harmonics from a 2-level PWM-process appear at sideband frequencies f_h around multiples of the switching frequency f_{sw}. according to:

$$f_h = nf_{sw} \pm mf_0, \tag{1}$$

where f_0 is the fundamental frequency, and n, m are integers [28]. The dominant phase-to-phase time harmonic components appear at $\{n = 1, m = 2\}$ and $\{n = 2, m = 1\}$. Since $f_{sw} >> f_0$ holds in this study, (1) can be simplified to $f_h \approx nf_{sw}$. A silicon-based inverter in the kW-range typically uses a switching frequency of around 10 kHz. The first two harmonic sideband groups take place around 10 and 20 kHz. A wide band-gap based inverter in the same power range would use a switching frequency of up to 50 kHz, resulting in the two first harmonic sideband groups taking place around 50 and 100 kHz. In order to cover both technologies, the investigated frequency range is chosen as 10-100 kHz in this study.

III. WINDING LOSS MODEL

Harmonic stator losses in electrical motors can be divided into winding copper losses P_w and stator lamination iron losses P_{lam}. Iron losses can thus be obtained by separating winding losses from measurements $P_{\text{lam}} = P_{\text{measured}} - P_w$. Therefore, accurate models for winding losses are required for the identification of iron losses. Loss models for Litz-wire windings have been developed in [29]–[34]. The orthogonality theorem presented in [31] allows separate treatment of skin and proximity effect losses in straight windings. The assumption is that the applied field due to proximity is uniform. Based on this assumption, the authors of [32] developed an analytical model for twisted litz-wire windings in transformers with good experimental agreement. The developed model was verified in a recent review [35]. Based on the same approach, the losses of Litz-wire windings P_w can be expressed in a more general form [33]:

$$P_w = k_{\text{skin}} R_{\text{DC}} I^2 \underbrace{- k_{\text{prox}} H_w^2}_{P_{\text{proximity}}}, \tag{2}$$

where R_{DC} is the DC resistance, I the RMS current and H_w is the winding RMS magnetic field strength. k_{skin} is the analytically determined skin effect factor according to [34]:

$$k_{\text{skin}} = \frac{\gamma}{2} \frac{ber\gamma\, bei'\gamma - bei\gamma\, ber'\gamma}{ber'^2\gamma + bei'^2\gamma} \quad \gamma = \frac{d_s}{\sqrt{2}\delta_{\text{Cu}}}, \tag{3}$$

where d_s is the strand diameter and δ_{Cu} the skin depth of copper. ber and bei are the real and imaginary parts of the modified Bessel function of first kind and zero order, respectively [36]. ber' and bei' are their respective derivatives. k_{prox} is the proximity effect factor according to [32], [33]:

$$k_{\text{prox}} = \frac{2\pi L_w N_s \rho_{\text{Cu}} d_s}{\delta_{\text{Cu}}} \frac{ber_2\gamma\, ber'\gamma - bei_2\gamma\, bei'\gamma}{ber^2\gamma + bei^2\gamma}, \tag{4}$$

where L_w is the winding length, N_s the total number of litz-wire strands and ρ_{Cu} the resistivity of copper. ber_2 and bei_2 are the real and imaginary parts the modified Bessel function of first kind and second order, respectively [32].

The model in (2) assumes ideal winding transposition. However, manufacturing variation in the turn-to-turn transposition may increase the losses [37], [38]. This effect is neglected in this study.

IV. IRON LOSS MODEL

No universal iron loss model can be found in the currently available literature. An overview of useful models is provided in [39], reporting that analytical models based on the Steinmetz equation [40] are considered best suited for rough post-processing estimations in electric machine design.

One widely deployed model for fundamental losses in SiFe-based laminations is the Bertotti three-term model [41]. The model separates losses into hysteresis, eddy-current and excess losses. Many attempts have been made to incorporate for harmonic losses into the Bertotti model [42]–[47]. In [44], the authors present a model for prediction of losses under arbitrary input using the Preisach model for improved estimation of minor loops, validated up to 2 kHz switching frequency.

A few papers, including [15] and [46], investigate iron losses up to 20 kHz, both reporting an increased loss estimation error with frequency, mainly related to skin effect. The lamination skin depth δ_{lam} is given by:

$$\delta_{\text{lam}} = \sqrt{\frac{\rho_{\text{lam}}}{\pi \mu_{\text{lam}} f}}, \tag{5}$$

where μ_{lam} is the lamination permeability, ρ_{lam} is the lamination resistivity and f the frequency. Skin effect takes place when the skin depth is shorter than the lamination thickness h_{lam}, i.e. $\delta_{\text{lam}} < h_{\text{lam}}$. For $\delta_{\text{lam}} << h_{\text{lam}}$, the heavily non-uniform flux density distributions in the laminations [36] not only affects the eddy-current loss component, but also have a significant effect on core reluctivity [48] as well as the hysteresis loss component [49]. A consequence is that the Bertotti model becomes non-physical, and therefore not to prefer. Several papers have proposed methods for incorporation of the non-uniform flux density effects into time-stepping 2D FEA, suggesting homogenization techniques of lamination stacks [50]–[54]. The same approach has also gained recognition when applied in the frequency domain [36], [55]. For small perturbations around a magnetic working point, core permeance in the frequency domain is characterized by the complex relative permeability $\mu_{r,e}$ [48], [56] according to:

$$\mu_{r,e} = \mu_{r,\Delta} \frac{\tanh\left(\gamma \frac{h_{\text{lam}}}{2}\right)}{\gamma \frac{h_{\text{lam}}}{2}}, \tag{6}$$

where $\gamma = \frac{1+j}{2\delta_{\text{lam}}}$ and $\mu_{r,\Delta} = \frac{1}{\mu_0}\frac{dB}{dH}$ is the local value of relative permeability. Thus, provided access to the low frequency B-H behavior, the permeance of laminated cores can be accurately determined over a very wide frequency range.

In this paper, the theory from [56] is combined with static 2D FEA to determine the harmonic magnetic flux density distributions in the stator iron and windings. The corresponding losses can subsequently be identified. The emphasis in this paper is not on developing a sophisticated iron loss model, but to develop an efficient methodology for quantification of iron losses in fully assembled stators. The identified stator lamination iron losses P_{lam} are for simplicity characterized with the original Steinmetz equation [40] according to:

$$P_{\text{lam}} = C_{\text{SE}}(f) B_{\text{lam}}^{\alpha} f^{\beta}, \tag{7}$$

where C_{SE}, $1 < \alpha < 2$ and $1 < \beta < 3$ are the parameters to be empirically determined. In this study, $\alpha = \beta = 2$ is assumed as an initial approach, while $C_{\text{SE}}(f)$ is determined for each frequency. B_{lam} is the stator iron RMS value of magnetic flux density, and f is the harmonic frequency.

TABLE III
2D FEA MODEL DATA

Mesh elements	6227
Simulation time	< 1s
Outer boundary condition	$A_z = 0$

V. METHOD

The rotor loss model previously developed by the authors in [13] treated pulsating magnetic flux generated by phase-to-phase connection of a single phase AC-supply. The same electrical connection has therefore been used in this paper.

Remark: The rotor is never present in this study since only stator losses are treated. The adopted methodology is described in Fig. 3. The power losses are measured under sinusoidal voltage excitation of the stator according to Fig. 3a, using the measurement setup in Fig. 4. The magnetic flux density distribution, required for separation of winding and core losses, is obtained by small-signal harmonic 2D FEA simulations in [57] using the measured RMS current I, and the lamination effective relative permeability $|\mu_{\text{r,e}}|$ as described in Fig. 3b. As can be seen, the reluctance of the magnetic flux path is dominated by the large relative airgap. Consequently, the small signal reluctance around a certain magnetic working point can be assumed as constant.

Thus, the resulting current waveform will be perfectly sinusoidal due to the large relative air gap, regardless of DC-bias saturation. The 2D FEA model stator yoke exterior boundary condition was set to magnetic insulation by defining the axial magnetic vector potential to zero, $A_z = 0$. Relevant 2D FEA model data are summarized in Table III. The lamination losses can finally be identified by subtracting the winding losses according to Fig. 3c. H_w is the winding average RMS magnetic field strength and B_{lam} is the stator core average RMS magnetic flux density, determined by:

$$H_w^2 = \frac{1}{A_w} \int_{r_w}^{r_{\text{si}}} \int_{0}^{\frac{\pi}{2}} H^2 \, \mathrm{d}\gamma \mathrm{d}r \quad B_{\text{lam}}^2 = \frac{1}{A_{\text{lam}}} \int_{r_{\text{si}}}^{r_{\text{so}}} \int_{0}^{\frac{\pi}{2}} B^2 \, \mathrm{d}\gamma \mathrm{d}r, \tag{8}$$

where $H = H(\gamma, r)$ and $B = B(\gamma, r)$ are obtained by static 2D FEA, and A denotes the integration area. The calculation of $|\mu_{\text{r,e}}|$ requires the incremental relative permeability $\mu_{r,\Delta}$. It was computed according to:

$$\mu_{r,\Delta} = \frac{1}{\mu_0} \frac{dB}{dH}. \tag{9}$$

where $\frac{dB}{dH}$ originates from the low-frequency characterization results presented in Section VII.

VI. MEASUREMENT SETUP

An overview of the measurement setup is provided in Fig. 3. The slotless stator (depicted in Figure 11a) was excited by a sinusoidal voltage according to the connection in Fig. 3a. The voltage was achieved by cascading a waveform generator with a linear power amplifier. The voltage and current data was aquired using a high bandwidth power meter. The sample temperature was logged using a T-type sensor glued to the

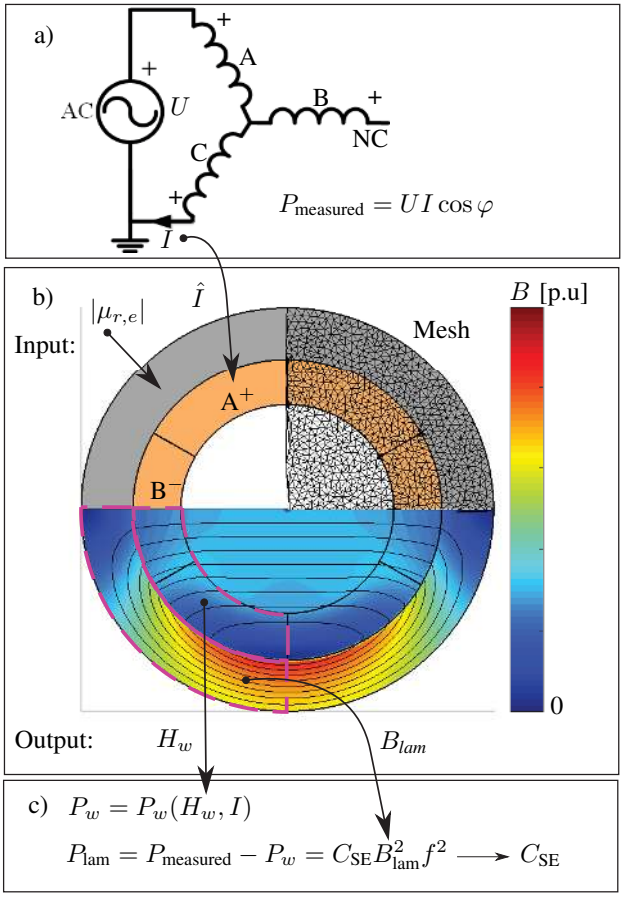

Fig. 3. Methodology workflow: a) Experimental connection; b) 2D FEA model for simulation of flux density distribution; c) Identifaction of lamination iron losses. *Remark: the rotor is never present in this study.*

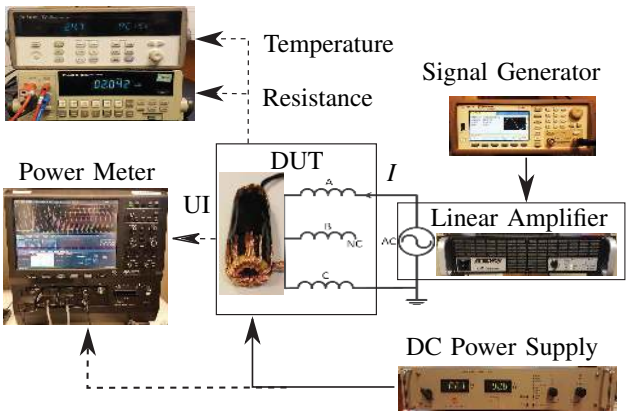

Fig. 4. Measurement setup

inside of the stator in the mid-axial position. All measurements were conducted at room temperature, 25°C. In order to accurately determine the stator winding losses, the phase-to-phase DC resistance R_{DC} was measured within seconds after each test, deploying the 4-wire method. The issue of creating an external DC-bias is a challenging task because of the potential transformer coupling between motor winding and an external excitation coil. The DC-bias was created by a litz-wire coil

TABLE IV
EQUIPMENT

Equipment type	Model
Waveform Generator	Agilent 33500B
Power Amplifier	AE Techtron 7224
Power Meter	Lecroy MDA 803
Voltage probe	HVD 3106
Current probe	CP031
Temperature logger	Agilent 34970A
Resistance meter	Fluke 8842A
Flux meter	Lakeshore 480
DC power supply	Delta Elektronika SM45-70D

(for minimal eddy-current losses) with 15 turns (CLI 200/120) depicted in Fig. 11b, fed by a DC supply. In order to ensure cancellation of the transformer coupling, the coil turns were uniformly distributed. The equipment involved are listed in Table IV.

A. Data collection

In order to minimize the thermal influence on measurements, each session was always preceded by an initial 2 hour turn-on of the measurement system. This allows potential settling in its characteristics. After each measurement session, a wide-band (10-100 kHz) characterization of the systematic error regarding amplitude and relative phase between the current and voltage measurement channels was made. The characterization used a 50 Ω, low-inductance temperature-stable power film-resistor (Caddock MP-915-50).

B. Data analysis

The harmonic power losses were computed according to

$$P_{\text{measured}}(f) = \frac{\hat{U}(f)\hat{I}(f)}{2}\cos\varphi, \tag{10}$$

where $\hat{U}$ is the measured peak voltage and $\hat{I}$ the measured peak current. $\hat{I}$ has been corrected with the amplitude characterization outlined above. Here, φ is the measured phase angle corrected with results obtained from characterization:

$$\varphi = \varphi_{\text{meas}}(f) - \Delta\varphi(f). \tag{11}$$

The variables were obtained using Fourier analysis of five consecutive harmonic periods at a sampling frequency of 2.5 Gs/s. $\Delta\varphi(f)$ was obtained during the characterization succeeding each measurement session. The measurements presented in this paper are characterized by almost inductive load conditions. It can be shown that the percentual power loss estimation error at these conditions is approximated by:

$$\Delta P_{\text{error}} \approx 100\frac{\sin(\varphi_{\text{error}})}{\cos(\varphi)}, \qquad [\%] \tag{12}$$

where φ is the actual phase angle, and φ_{error} is the systematic angular measurement error. The angular precision was determined by conducting 20 characterization measurements (using the low-inductive power film resistor) at each frequency, using input voltage in the range 10-25 V_{RMS}. φ_{error} was determined to below 0.15° over the whole frequency range with 95 % confidence bounds.

C. Outline of results

The stator steel B-H relationships are characterized in Section VII. The winding loss models are validated in Section VIII and iron losses are determined in Section IX. All power loss measurements presented in this paper have been conducted without the rotor, and corrected with characterization results.

VII. Stator steel B-H characterization

A stator core sample is illustrated in Fig. 5. As can be seen in Fig. 6, the stator ring cores were excited using a coil fed by a controllable DC-supply (Delta Elektronika SM45-70D). In order to be able to saturate the cores using the DC-supply, N_e =10 turns were needed, and a large wire diameter was required to handle the peak currents (AWG 15). The resulting magnetic field was determined according to:

$$H_{\text{lam}} = \frac{N_e I_{DC}}{2\pi r_{\text{s,av}}} \tag{13}$$

where $r_{\text{s,av}} = \frac{r_{\text{so}} - r_{\text{si}}}{2}$ is the average stator lamination radius and I_{DC} is the applied DC current. The flux was measured via a 44 turn search-coil connected to a fluxmeter. Since the search coil currents are negligible, a thinner wire diameter was chosen (AWG 24). The number of search coil turns were maximized with reference to the stator core inner diameter for maximal accuracy. In order to minimize the impact of eddy-currents on results, the rate of change of magnetic flux density was kept below $\frac{dB}{dt} < 3$ T/s. In order to investigate the minor loop

Fig. 5. Stator core.

Fig. 6. Stator core equipped with a) Search coil; b) Excitation coil. *Remark: Only used for characterization of B-H relationship.*

behavior, an arbitrary waveform generator was cascaded with the DC-supply. 4 consecutive sinusoidal minor loops (45 A/m amplitude) at low frequency under incrementally increasing level DC-bias were programmed. The results (illustrated in Fig. 7) show that the minor loop relative permeabilities are significantly lower than the fundamental ones (up to 6 times) depending on the level of DC-bias. The results also show that the minor loops are reversible and follow an almost linear B-H relationship for small perturbations around a certain level of DC-bias. The obtained minor loop incremental relative permeabilities (using the small-signal linearization described in Fig. 7), are summarized in Fig. 8 as function of DC-bias.

VIII. Winding loss model validation

In order to validate the winding loss model in (2), the losses of a separate phase-coil (Fig. 10a) far from any other conductive objects, were measured at 50 V RMS input at 25 and 85°C. The results are shown in Fig. 9a. At 10 kHz, the

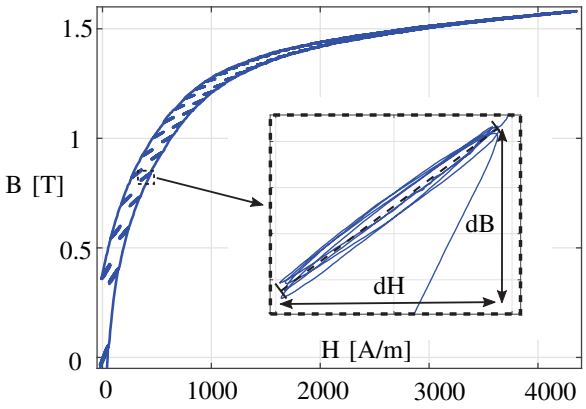

Fig. 7. Obtained B-H curve for the NO20 stator core.

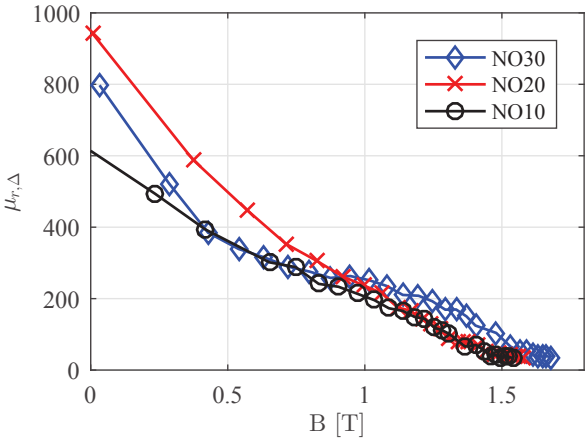

Fig. 8. Minor loop relative permeabilities as function of DC-bias.

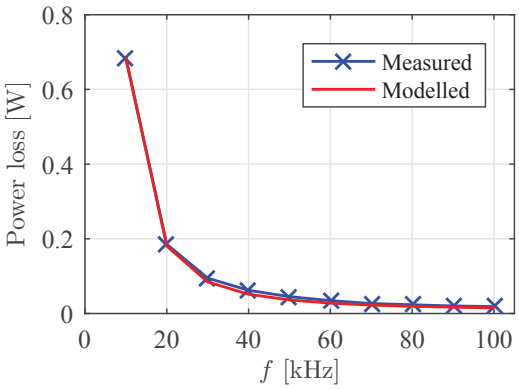

Fig. 9. Losses of a separate phase coil in airgap at 50 V RMS input.

difference was less than 5 % for both temperatures. At 100 kHz, measured losses were 15 % higher than modeled ones for both temperatures. According to the model, proximity losses dominate beyond 70 kHz. The model for proximity losses assumes ideal transposition. Thus, one possible reason to the increased relative difference between modelled and measured losses is non-ideal manufacturing effects. The magnetic field in

the coil, necessary to compute proximity losses, was obtained by 2D FEA according to the methodology described in Fig. 3.

A. Winding proximity losses

The winding proximity loss expression $P_{\text{proximity}}$ in (2) was validated by measuring the additional losses of a separate phase-coil (see Fig. 10b) placed in the middle of the airgap (see Fig. 10a), when applying a sinusoidal input voltage of 50 V. H_w was obtained from 2D finite-element simulations. The obtained results presented in Fig 12 show that measured losses were within 15 % of the predicted ones. Thus, the results validate the expression for $P_{\text{proximity}}$ in (2).

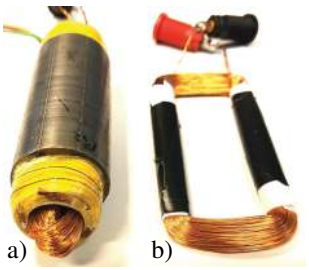

Fig. 10. a) Separate phase-coil inside the stator airgap; b) Separate phase-coil.

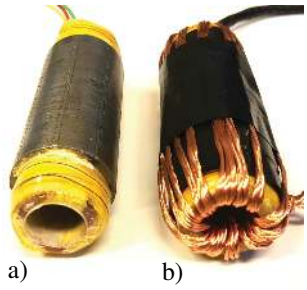

Fig. 11. a) Stator; b) stator with DC-bias coil for AC power loss measurement.

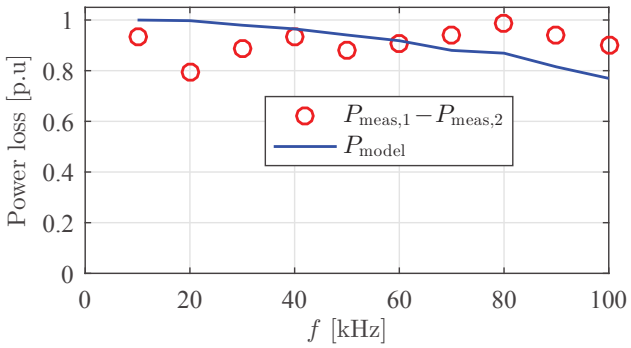

Fig. 12. Losses of separate phase coil in airgap at 50 V RMS input.

IX. Iron Losses

In this and the following sections, lamination losses P_{lam} have been identified by subtracting winding losses P_w from the measured losses according to $P_{lam} = P_{\text{measured}} - P_w$, using the method described in Fig. 3. All measurements were conducted at room temperature (25°C), using a sinusoidal AC input with constant voltage amplitude. The winding losses P_w and stator yoke relative permeability $\mu_{r,e}$ were computed according to equations (2) and (6), respectively. The remainder after this subtraction are considered as the lamination iron losses. Iron losses in three different steel grades are identified with, and without external DC-bias in Sections IX-A and IX-B, respectively.

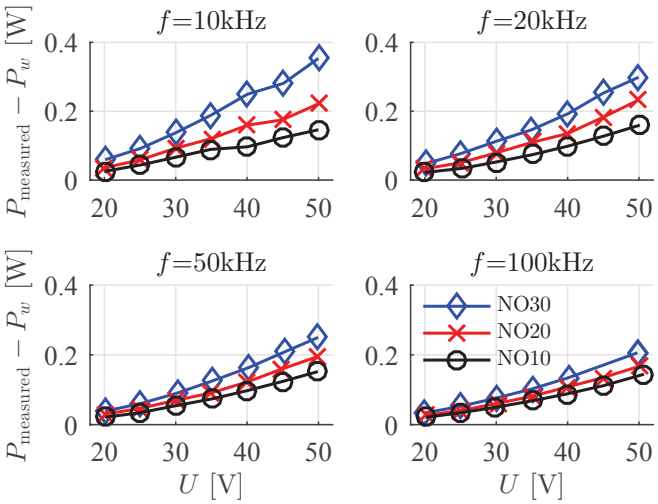

Fig. 13. Iron losses from measurements, NO10-NO30, variable RMS input voltage range.

A. Stator yoke iron losses without external DC-bias

Fig. 13 shows the measured iron losses of all three considered stator steel grades at 10, 20, 50 and 100 kHz. The results show that iron losses increase quadratically with input voltage. Further, losses can be more than halved at 10 kHz by using NO10 instead of NO30. However, the benefit of thinner lamination (at zero DC-bias) decreases with frequency. At 100 kHz, iron losses are only reduced by 30 % by using NO10 instead NO30. Further, measured losses at 10 kHz are twice as high compared to Epstein-frame based loss modelling (provided by the manufacturer). Unfortunately, no manufacturer data is available for higher frequencies.

B. Impact of DC-bias on stator iron losses

In this section, the impact of a DC-bias magnetic field on the stator lamination iron losses has been investigated at 50 V AC input. The bias was achieved by the external excitation coil depicted in Fig. 11b and its resulting magnetic field was calculated according to (13). The additional eddy-current losses taking place in the external coil have been subtracted from the total losses using the expression for $P_{w,e}$ in equation (2). The external coil is assumed to give uprise to a homogeneous magnetic field distribution in the stator yoke.

Fig. 14 shows the iron losses of an NO20 stator when subjected to a DC-bias (0–1.6 T), for a set of frequencies. Measured iron losses exhibit a weak dependency of DC-bias from 0-1 T, whereafter an increase can be observed until 1.5 T where the losses peak (regardless of frequency). As can be seen, the impact of DC-bias on iron losses can be significant. At 10 kHz, losses are 50 % higher at 1.4 T than at 1.6 T DC-bias. The same phenomena was observed for NO10 and NO30. One explanation can be found in the nature of iron losses in SiFe steel under DC-biased condition, since both eddy current and hysteresis losses depend on the DC-bias level [23], [24], [58].

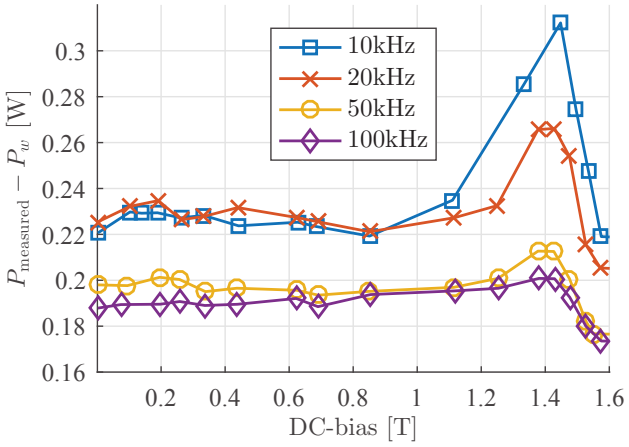

Fig. 14. NO20 losses at different DC-bias, 50V RMS input.

C. Iron loss characterization

In this section, the iron losses of three steel grades are characterized using the Steinmetz equation expressed in (7). Due to the previously observed dependency of stator losses with DC-bias, three different saturation levels have been chosen: 0, 100 and 1000 A/m, correspondong to approximately 0, 0.2 and 1.4 T, respectively. In order to investigate any dependency of iron losses on AC amplitude, an input range of 20-50 V_{RMS} has been used. The Steinmetz coefficient C_{SE} is identified for each frequency and saturation level, using data from the whole input voltage range according to:

$$\overline{C}_{\text{SE}}(f) = \frac{1}{N} \sum_{U=U_1}^{U_N} C_{\text{SE}}(U, f), \tag{14}$$

where

$$C_{\text{SE}}(U, f) = \frac{P_{\text{measured}}(f, U) - P_w(f, U)}{f^2 B^2_{\text{lam}}(f, U)} \tag{15}$$

is determined using the procedure described in Fig. 3. The obtained Steinmetz coefficients for all steel grades are shown in Fig. 15 for the three saturation levels. The obtained loss coefficients are clearly higher (up to 30 %) at 1.4 T than 0.2 T DC-bias.

The iron loss coefficients decrease until 70 kHz in Fig. 15. Similar decreases with frequency have been demonstrated in [15]–[17]. They are commonly explained by decreasing eddy-current losses due to the skin effect. However, the following increase in iron losses beyond a certain frequency has been more sparsely discussed. The authors of [17] make a similar observation and mention increasing deadtime as one possible reason. The same explanation can be excluded in this study due to perfectly sinusoidal waveforms as discussed in Section V. However, the hysteresis losses have been reported to increase due to: **a)** the increasingly non-uniform flux density distribution with frequency itself [49]; **b)** the increasing amount of magnetic flux passing through deteriorated regions due to the field displacement towards lamination surfaces [19]–[22].

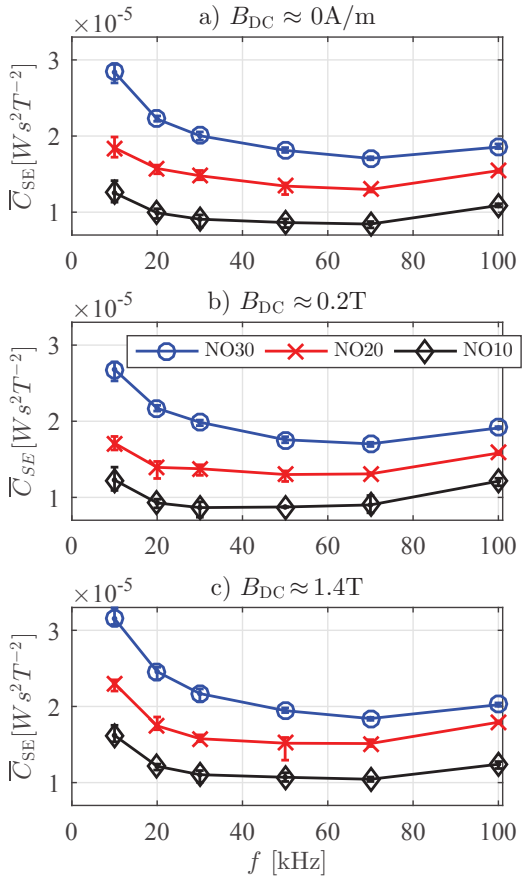

Fig. 15. $\overline{C}_{\text{SE}}$, NO10, NO20 and NO30 at different DC-bias level.

X. Discussion

In this section, the results are summarized and the model validity is discussed in Section X-A. The modelled and measured stator losses (normalized by NO20 losses at 10 kHz and 1.4 T) are compared in Fig. 16. Results show that harmonic stator losses can be reduced by more than three quarters by using 50 kHz switching frequency instead of 10 kHz. This

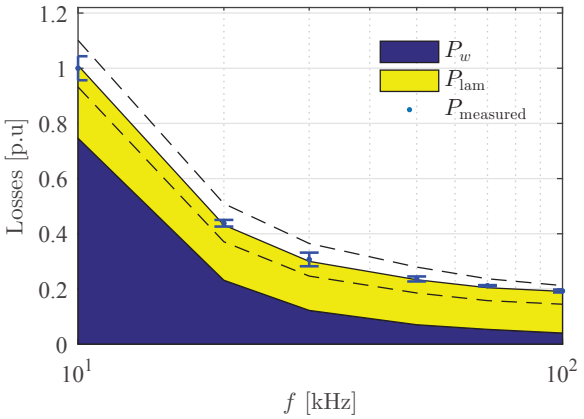

Fig. 16. Normalized NO20 stator losses at 50 V RMS input and approximately 1.4 T DC-bias. Error-bars show the 95 % confidence bounds for measured values. The dashed lines show the corresponding iron losses of NO10 (lower line) and NO30 (upper line).

TABLE V
EFFECTIVE RELATIVE PERMEABILITIES $\mu_{r,e}$ AT 100 KHZ.

	NO10	NO20	NO30
$B_{\mathrm{DC}} \approx 0.4$ T	376	225	117
$B_{\mathrm{DC}} \approx 1.5$ T	40	44	61

is due to the decrease of winding losses P_w with increased frequency. Beyond 50 kHz, copper conduction losses become negligible while iron losses dominate regardless of steel grade.

A. Model validity

As can be seen in Fig. 3, the harmonic magnetic flux path is not only tangential to the lamination surfaces, but also radially oriented. However, the material minor loop relative permeabilites reported in Section VII were measured under tangential flux orientation. The impair of magnetic properties due to cutting [19], [20], may result in a subsequent overestimation of the modeled magnetic flux densities. The consequence would be an incorrect loss separation and a subsequent underestimation of iron loss coefficients. Therefore, the influence of lamination relative permeability on normalized RMS flux density levels is shown in Fig. 17. As can be seen, the influence is less than 10 % for $\mu_{r,lam} > 30$. This insensitivity is explained by the large relative air gap as previously discussed in Section V. However, it also shows that the model sensitivity increases with DC-bias due to decreasing relative permeability when approaching saturation. The effective relative permeabilities at 100 kHz of the investigated materials are summarized in Table V at two different saturation levels. An assumed overestimation (in the upper range) of relative permeability by 30% (due to the neglection of radially oriented flux) at 1.5 T DC-bias would result in a corresponding overestimation of magnetic flux densities by less than 2 %. The resulting error on winding losses and iron loss coefficients would be less than 4 %. Thus, the modeling approach is considered sufficiently valid for the present study.

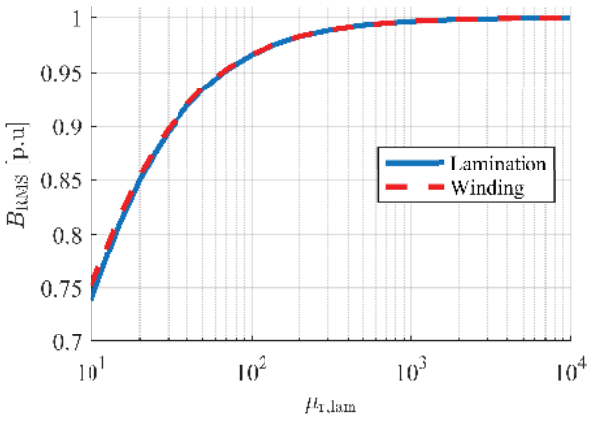

Fig. 17. Influence of lamination relative permeability on stator flux densities.

XI. CONCLUSION

The harmonic losses in three fully assembled stators of different steel grade (NO10, NO20 and NO30) of a 2-pole slotless permanent magnet motor have been measured. The analysis covers a wide frequency range (10-100 kHz) at different levels of DC-bias (up to $B_{\mathrm{lam}} \approx$1.6 T). For this purpose, the minor loop B-H relationships were characterized under incrementally increasing DC-bias. The winding loss models necessary for separation of iron losses were successfully validated using an innovative method. Measured iron losses are twice as high at 10 kHz compared to Epstein test results. This emphasizes the need to incorporate manufacturing influence on iron losses at high frequencies. At 10 kHz, iron losses can be roughly halved by using NO10 instead of NO30. The same substitution at 100 kHz only results in a decrease with 30 %. The effect of DC-bias was more significant at low than high frequencies. At 10 kHz, NO20 iron losses at $\approx$ 1.4 T DC-bias were 30 % higher than at $\approx$ 0.2 T. The proposed method enables fast and accurate access to harmonic iron losses at high frequencies. It is not only of direct importance for validation of harmonic motor loss models, but also useful for studies on manufacturing influence on iron losses. The developed models and aquired results contribute to the authors strive for a complete harmonic loss model of inverter-fed slotless motors. Subsequently, future work includes utilizing the proposed stator-loss model to accurately separate rotor losses in a complete, converter-fed machine.

ACKNOWLEDGMENT

The authors would like to thank Martin Sigrand, Erik Baker and Fredrik Zachrisson at Atlas Copco Industrial Technique AB in Nacka, Sweden for making this study possible.

REFERENCES

[1] B. Y. F. Luise, A. Tessarolo, F. Agnolet, S. Pieri, M. Scalabrin, M. D. I. Chiara, and M. D. E. Martin, "Design Optimization and Testing of High-Performance Motors," *IEEE Ind. Appl. Mag.*, no. 6, pp. 19–32, 2016.

[2] S. Jumayev, K. O. Boynov, J. J. H. Paulides, E. A. Lomonova, and J. Pyrhonen, "Slotless PM Machines with Skewed Winding Shapes: 3-D Electromagnetic Semianalytical Model," *IEEE Trans. Magn.*, vol. 52, no. 11, pp. 1–12, 2016.

[3] P. D. Pfister and Y. Perriard, "Very-high-speed slotless permanent-magnet motors: Analytical modeling, optimization, design, and torque measurement methods," *IEEE Trans. Ind. Electron.*, vol. 57, no. 1, pp. 296–303, 2010.

[4] C. Zwyssig, J. W. Kolar, and S. D. Round, "Megaspeed drive systems: Pushing beyond 1 million r/min," *IEEE/ASME Trans. Mechatronics*, vol. 14, no. 5, pp. 564–574, 2009.

[5] O. Wallmark, P. Kjellqvist, and F. Meier, "Analysis of axial leakage in high-speed slotless PM motors for industrial hand tools," *IEEE Trans. Ind. Appl.*, vol. 45, no. 5, pp. 1815–1820, 2009.

[6] N. Bianchi, S. Bolognani, and F. Luise, "High speed drive using a slotless PM motor," *PESC Rec. - IEEE Annu. Power Electron. Spec. Conf.*, vol. 1, no. 4, pp. 458–463, 2004.

[7] J. Millinger, O. Wallmark, and J. Soulard, "Influence of Lamination Thickness on Harmonic Losses in 2-pole Slotless Permanent-Magnet Motors," in *IEEE Int. Electr. Mach. Drives Conf. (IEMDC)*, pp. 1–6, 2017.

[8] N. Bianchi, S. Bolognani, and F. Luise, "Potentials and limits of high speed PM motors," *38th IAS Annu. Meet. Conf. Rec. Ind. Appl. Conf.*, vol. 3, no. 6, pp. 1570–1578, 2003.

[9] H. Di, L. Yingjie, and B. Sarlioglu, "Analysis of SiC based power electronic inverters for high speed machines," in *Appl. Power Electron. Conf. Expo.*, pp. 304–310, 2015.

[10] L. Schwager, A. Tuysuz, C. Zwyssig, and J. W. Kolar, "Modeling and comparison of machine and converter losses for PWM and PAM in high-speed drives," *IEEE Trans. Ind. Appl.*, vol. 50, no. 2, pp. 995–1006, 2014.

[11] A. Krings, J. Soulard, and O. Wallmark, "PWM Influence on the Iron Losses and Characteristics of a Slotless Permanent-Magnet Motor With SiFe and NiFe Stator Cores," *IEEE Trans. Ind. Appl.*, vol. 51, no. 2, pp. 1475–1484, 2015.

[12] J. Millinger and J. Soulard, "Energy-Efficiency of Electrical Machine and Drive with SiC Transistors (2015-03073)," Tech. Rep., 2016. [Online]. Available: urn:nbn:se:kth:diva-212295

[13] J. Millinger, J. Soulard, and O. Wallmark, "Influence of Shaft Relative Permeability on Rotor Losses in 2-pole Slotless High-Speed Motor," in *XXII Int. Conf. Electr. Mach.*, pp. 407–413, 2016.

[14] A. Krings, "Iron losses in electrical machines - Influence of material properties, manufacturing processes and inverter operation," Ph.D. dissertation, KTH Royal Institute of Technology, 2014.

[15] A. Boglietti, P. Ferraris, M. Lazzari, and M. Pastorelli, "Change of the Iron Losses with the Switching Supply Frequency in Soft Magnetic Materials Supplied by PWM Inverter," *IEEE Trans. Magn.*, vol. 31, no. 6, pp. 4250–4252, 1995.

[16] M. Taghizadeh Kakhki, J. Cros, and P. Viarouge, "New Approach for Accurate Prediction of Eddy Current Losses in Laminated Material in the Presence of Skin Effect with 2-D FEA," *IEEE Trans. Magn.*, vol. 52, no. 3, pp. 3–6, 2016.

[17] W. Martinez, S. Odawara, and K. Fujisaki, "Iron Loss Characteristics Evaluation Using a High Frequency GaN Inverter Excitation," *accepted for publication in IEEE Trans. Magn.*, no. 1, pp. 1–8, 2017.

[18] T. L. Mthombeni, P. Pillay, and R. M. W. Strnat, "New Epstein Frame for Lamination Core Loss Measurements Under High Frequencies and High Flux Densities," vol. 22, no. 3, pp. 614–620, 2007.

[19] K. Bourchas, A. Stening, J. Soulard, A. Broddefalk, M. Lindenmo, M. Dahlén, and F. Gyllensten, "Influence of Cutting and Welding on Magnetic Properties of Electrical Steels," in *XXII Int. Conf. Electr. Mach.*, pp. 1817–1823, 2016.

[20] W. M. Arshad, T. Ryckebusch, F. Magnussen, H. Lendenmann, B. Eriksson, J. Soulard, and B. Malmros, "Incorporating Lamination Processing and Component Manufacturing in Electrical Machine Design Tools," *2007 IEEE Ind. Appl. Annu. Meet.*, pp. 94–102, 2007.

[21] A. Krings, S. Nategh, O. Wallmark, and J. Soulard, "Influence of the Welding Process on the Performance of Slotless PM motors with SiFe and NiFe Stator Laminations," *IEEE Trans. Ind. Appl.*, vol. 50, no. 1, pp. 296–306, 2014.

[22] H. Wang and Y. Zhang, "Modeling of Eddy Current Losses of Welded Laminated Electrical Steels," *IEEE Trans. Ind. Electron.*, vol. PP, no. 99, pp. 1–9, 2016.

[23] T. Taitoda, Y. Takahashi, and K. Fujiwara, "Iron Loss Estimation Method for a General Hysteresis Loop With Minor Loops," vol. 51, no. 11, 2015.

[24] B. Tekgun, Y. Sozer, and I. Tsukerman, "Measurement of core losses in electrical steel in the saturation region under DC bias conditions," *IEEE Trans. Ind. Appl.*, vol. 53, no. 1, pp. 276–282, 2015.

[25] Published data sheets from Cogent Power, 2017. [Online]. Available: https://cogent-power.com/downloads

[26] N. Bernard, F. Martin, and M. E.-h. Za, "Design Methodology of a Permanent Magnet Synchronous Machine for a Screwdriver Application," vol. 27, no. 3, pp. 624–633, 2012.

[27] A. G. Gonzalez, "Magnet Losses in Inverter-fed High-speed PM Machines," M.S thesis, KTH Royal Institute of Technology, 2015.

[28] T. Lipo and D. G. Holmes, *Pulse Width Modulation for Power Converters*, 1st ed. Wiley-IEEE Press, 2003.

[29] P. L. Dowell, "Effects of Eddy Currents in Transformer Windings," *Proc. Inst. Electr. Eng.*, vol. 113, no. 8, pp. 1387–1394, 1966.

[30] R. L. Stoll, *The analysis of eddy currents*, ser. Monographs in electrical and electronic engineering. Clarendon Press, 1974.

[31] J. A. Ferreira, "Improved Analytical Modeling of Conductive Losses in Magnetic Components," *IEEE Trans. Power Electron.*, vol. 9, no. I, pp. 127–131, 1994.

[32] M. Bartoli, N. Noferi, A. Reatti, and V. S. Marta, "Modeling Litz-Wire Winding Losses in High-Frequency Power Inductors," in *Power Electron. Spec. Conf. PESC '96*, pp. 1690–1696, 1996.

[33] F. Tourkhani and P. Viarouge, "Accurate Analytical Model of Winding Losses in Round Litz Wire Windings," *IEEE Trans. Magn.*, vol. 37, no. 1, pp. 538–543, 2001.

[34] A. V. den Bossche, *Power Inductors and Transformers for Power Electronics*. CRC Press, 2005.

[35] V. Vaisanen, J. Hiltunen, J. Nerg, and P. Silventoinen, "AC Resistance Calculation Methods and Practical Design Considerations When Using Litz Wire," *39th Annu. Conf. Ieee Ind. Electron. Soc. (Iecon 2013)*, pp. 368–375, 2013.

[36] M. K. Kazimierczuk, *High-Frequency Magnetic Components*, 2nd ed. Wiley Interscience, 2014.

[37] P. B. Reddy, T. M. Jahns, and T. P. Bohn, "Transposition Effects on Bundle Proximity Losses in High-Speed PM Machines," *2009 IEEE Energy Convers. Congr. Expo. ECCE 2009*, no. 1, pp. 1919–1926, 2009.

[38] C. R. Sullivan, R. Y. Zhang, and C. Sci, "Analytical Model for Effects of Twisting on Litz-Wire Losses," in *Control Model. Power Electron.*, pp. 1–10, 2014.

[39] A. Krings and J. Soulard, "Overview and Comparison of Iron Loss Models for Electrical Machines," *J. Electr. Eng.*, vol. 10, pp. 162–169, 2010.

[40] C. P. Steinmetz, "On the Law of Hysteresis," *Trans. Am. Inst. Electr. Eng.*, vol. IX, no. 1, pp. 3–64, 1892.

[41] G. Bertotti, "General Properties of Power Losses in Soft Ferromagnetic Materials." *IEEE Trans. Magn.*, vol. 24, no. 1, pp. 621–630, 1987.

[42] M. Amar and R. Kaczmarek, "A General Formula for Prediction of Iron Losses Under Nonsinusoidal Voltage Waveform," *IEEE Trans. Magn.*, vol. 31, no. 5, pp. 2504–2509, 1995.

[43] A. Boglietti, A. Cavagnino, M. Lazzari, and M. Pastorelli, "Predicting Iron Losses in Soft Magnetic Materials With Arbitrary Voltage Supply: An Engineering Approach," *IEEE Trans. Magn.*, vol. 39, no. 2, pp. 981–989, 2003.

[44] E. Barbisio, F. Fiorillo, and C. Ragusa, "Predicting Loss In Magnetic Steels Under Arbitrary Induction Waveform and With Minor Hysteresis Loops," *IEEE Trans. Magn.*, vol. 40, no. 4 I, pp. 1810–1819, 2004.

[45] Z. Gmyrek, A. Boglietti, and A. Cavagnino, "Iron Loss Prediction With PWM Supply Using Low- and High-Frequency Measurements: Analysis and Results Comparison," *IEEE Trans. Ind. Electron.*, vol. 55, no. 4, pp. 1722–1728, 2008.

[46] M. Popescu, D. M. Ionel, A. Boglietti, A. Cavagnino, C. Cossar, and M. I. McGilp, "A General Model for Estimating the Laminated Steel Losses Under PWM Voltage Supply," *IEEE Trans. Ind. Appl.*, vol. 46, no. 4, pp. 1389–1396, 2010.

[47] M. J. Hofmann and H. G. Herzog, "Modeling Magnetic Power Losses in Electrical Steel Sheets in Respect of Arbitrary Alternating Induction Waveforms: Theoretical Considerations and Model Synthesis," *IEEE Trans. Magn.*, vol. 51, no. 2, pp. 1–11, 2015.

[48] K. Abeywickrama, T. Daszczynski, Y. V. Serdyuk, and S. M. Gubanski, "Determination of Complex Permeability of Silicon Steel for Use in High-Frequency Modeling of Power Transformers," *IEEE Trans. Magn.*, vol. 44, no. 4, pp. 438–444, 2008.

[49] K. Yamazaki and N. Fukushima, "Iron Loss Model for Rotating Machines Using Direct Eddy Current Analysis in Electrical Steel Sheets," *IEEE Trans. Energy Convers.*, vol. 25, no. 3, pp. 633–641, 2010.

[50] W. Legros, S. Tilman, and I. Introduction, "Calculation of Eddy Currents and Associated Losses in Electrical Steel Laminations," *IEEE Trans. Magn.*, vol. 35, no. 3, pp. 1191–1194, 1999.

[51] P. Dular, J. Gyselinck, C. Geuzaine, N. Sadowski, and J. P. A. Bastos, "A 3-D Magnetic Vector Potential Formulation Taking Eddy Currents in Lamination Stacks Into Account," *IEEE Trans. Magn.*, vol. 39, no. 3, pp. 1424–1427, 2003.

[52] J. Gyselinck, P. Dular, and A. P. Flux, "A Time-Domain Homogenization Technique for Laminated Iron Cores in 3-D Finite-Element Models," *IEEE Trans. Magn.*, vol. 40, no. 2, pp. 856–859, 2004.

[53] J. Gyselinck, R. V. Sabariego, and P. Dular, "A Nonlinear Time-Domain Homogenization Technique for Laminated Iron Cores in Three-Dimensional Finite-Element Models," *IEEE Trans. Magn.*, vol. 42, no. 4, pp. 763–766, 2006.

[54] O. Bottesi, L. Alberti, R. V. Sabariego, and J. Gyselinck, "Finite Element Small-Signal Simulation of Electromagnetic Devices Considering Eddy Currents in the Laminations," *IEEE Trans. Magn.*, vol. 53, no. 5, pp. 1–8, 2017.

[55] G. Buchgraber, "Complex Representation in Nonlinear Time Harmonic Eddy Current Problems," *IEEE Trans. Magn.*, vol. 34, no. 5, pp. 2–5, 1998.

[56] D. Roger, E. Napieralska-Juszczak, and A. Henneton, "High Frequency Extension of Non-Linear Models of Laminated Cores," *Int. J. Comput. Math. Electr. Electron. Eng.*, vol. 26, no. 4, pp. 986–1004, 2006.

[57] D. Meeker, "Finite element method magnetics, version 4.2," 2013. [Online]. Available: http://www.femm.info

[58] A. M. Knight, J. C. Salmon, and J. Ewanchuk, "Integration of a first order eddy current approximation with 2D FEA for prediction of PWM harmonic losses in electrical machines," *IEEE Trans. Magn.*, vol. 49, no. 5, pp. 1957–1960, 2013.